Title

Multimodal in vivo imaging of oral cancer using fluorescence lifetime, photoacoustic and ultrasound techniques.

Journal

Biomedical Optics Express, 4(9)

ISSN

2156-7085

Authors

Fatakdawala, Hussain

Poti, Shannon

Zhou, Feifei

et al.

Publication Date

2013-09-01

DOI

10.1364/boe.4.001724

Peer reviewed

Biomedical Optics EXPRESS

Multimodal *in vivo* imaging of oral cancer using fluorescence lifetime, photoacoustic and ultrasound techniques

Hussain Fatakdawala,[1] Shannon Poti,[2] Feifei Zhou,[1] Yang Sun,[1] Julien Bec,[1] Jing Liu,[1] Diego R. Yankelevich,[1,3] Steven P. Tinling,[3] Regina F. Gandour-Edwards,[4] D. Gregory Farwell,[2] and Laura Marcu[1,*]

[1] *Department of Biomedical Engineering, University of California-Davis, Davis, CA 95616, USA*
[2] *Department of Otolaryngology, University of California-Davis, Sacramento, CA 95817, USA*
[3] *Department of Electrical Engineering, University of California-Davis, Davis, CA 95616, USA*
[4] *Department of Pathology & Laboratory Medicine, University of California-Davis, Sacramento, CA 95817, USA*
**lmarcu@ucdavis.edu*

Abstract: This work reports a multimodal system for label-free tissue diagnosis combining fluorescence lifetime imaging (FLIm), ultrasound backscatter microscopy (UBM), and photoacoustic imaging (PAI). This system provides complementary biochemical, structural and functional features allowing for enhanced in vivo detection of oral carcinoma. Results from a hamster oral carcinoma model (normal, precancer and carcinoma) are presented demonstrating the ability of FLIm to delineate biochemical composition at the tissue surface, UBM and related radiofrequency parameters to identify disruptions in the tissue microarchitecture and PAI to map optical absorption associated with specific tissue morphology and physiology.

OCIS codes: (300.6500) Spectroscopy, time-resolved; (170.7180) Ultrasound diagnostics; (170.5120) Photoacoustic imaging; (170.3880) Medical and biological imaging.

References and links

1. R. Siegel, D. Naishadham, and A. Jemal, "Cancer statistics, 2013," CA Cancer J. Clin. **63**(1), 11–30 (2013).
2. L. Martí-Bonmatí, R. Sopena, P. Bartumeus, and P. Sopena, "Multimodality imaging techniques," Contrast Media Mol. Imaging **5**(4), 180–189 (2010).
3. Y. Sun, H. Xie, J. Liu, M. Lam, A. J. Chaudhari, F. Zhou, J. Bec, D. R. Yankelevich, A. Dobbie, S. L. Tinling, R. F. Gandour-Edwards, W. L. Monsky, D. G. Farwell, and L. Marcu, "*In vivo* validation of a bimodal technique combining time-resolved fluorescence spectroscopy and ultrasonic backscatter microscopy for diagnosis of oral carcinoma," J. Biomed. Opt. **17**(11), 116003 (2012).
4. W. J. Hucker, C. M. Ripplinger, C. P. Fleming, V. V. Fedorov, A. M. Rollins, and I. R. Efimov, "Bimodal biophotonic imaging of the structure-function relationship in cardiac tissue," J. Biomed. Opt. **13**(5), 054012 (2008).
5. M. Niedre and V. Ntziachristos, "Elucidating Structure and Function In Vivo With Hybrid Fluorescence and Magnetic Resonance Imaging," Proc. IEEE **96**(3), 382–396 (2008).
6. V. Kalchenko, N. Madar-Balakirski, I. Meglinski, and A. Harmelin, "In vivo characterization of tumor and tumor vascular network using multi-modal imaging approach," J Biophotonics **4**(9), 645–649 (2011).
7. N. Howlader, A. M. Noone, M. Krapcho, N. Neyman, R. Aminou, S. F. Altekruse, C. L. Kosary, J. Ruhl, Z. Tatalovich, H. Cho, A. Mariotto, M. P. Eisner, D. R. Lewis, H. S. Chen, E. J. Feuer, and K. A. Cronin, eds., "SEER Cancer Statistics Review, 1975-2009 (Vintage 2009 Populations)," (National Cancer Institute., Bethesda, MD, 2012).
8. Z. Rumboldt, T. A. Day, and M. Michel, "Imaging of oral cavity cancer," Oral Oncol. **42**(9), 854–865 (2006).
9. B. M. Trotta, C. S. Pease, J. J. Rasamny, P. Raghavan, and S. Mukherjee, "Oral cavity and oropharyngeal squamous cell cancer: key imaging findings for staging and treatment planning," Radiographics **31**(2), 339–354 (2011).
10. W. L. Lodder, H. J. Teertstra, I. B. Tan, F. A. Pameijer, L. E. Smeele, M. L. F. van Velthuysen, and M. W. M. van den Brekel, "Tumour thickness in oral cancer using an intra-oral ultrasound probe," Eur. Radiol. **21**(1), 98–106 (2011).

#193145 - $15.00 USD Received 1 Jul 2013; revised 9 Aug 2013; accepted 9 Aug 2013; published 26 Aug 2013

11. M. Hagiwara, A. Nusbaum, and B. L. Schmidt, "MR Assessment of Oral Cavity Carcinomas," Magn. Reson. Imaging Clin. N. Am. **20**(3), 473–494 (2012).
12. L. L. Simon and D. Rubinstein, "Imaging of oral cancer," Otolaryngol. Clin. North Am. **39**(2), 307–317, vi (2006).
13. L. L. Myers, M. K. Wax, H. Nabi, G. T. Simpson, and D. Lamonica, "Positron Emission Tomography in the Evaluation of the N0 Neck," Laryngoscope **108**(2), 232–236 (1998).
14. D. Shin, N. Vigneswaran, A. Gillenwater, and R. Richards-Kortum, "Advances in fluorescence imaging techniques to detect oral cancer and its precursors," Future Oncol. **6**(7), 1143–1154 (2010).
15. J. C. Kah, K. W. Kho, C. G. Lee, C. James, R. Sheppard, Z. X. Shen, K. C. Soo, and M. C. Olivo, "Early diagnosis of oral cancer based on the surface plasmon resonance of gold nanoparticles," Int. J. Nanomedicine **2**(4), 785–798 (2007).
16. W. G. Jung, J. Zhang, J. R. Chung, P. Wilder-Smith, M. Brenner, J. S. Nelson, and Z. P. Chen, "Advances in oral cancer detection using optical coherence tomography," IEEE J Sel Top Quantum Electron. **11**(4), 811–817 (2005).
17. C.-K. Lee, T.-T. Chi, C.-T. Wu, M.-T. Tsai, C.-P. Chiang, and C.-C. Yang, "Diagnosis of oral precancer with optical coherence tomography," Biomed. Opt. Express **3**(7), 1632–1646 (2012).
18. P.-C. Li, C.-R. C. Wang, D.-B. Shieh, C.-W. Wei, C.-K. Liao, C. Poe, S. Jhan, A.-A. Ding, and Y.-N. Wu, "In vivo photoacoustic molecular imaging with simultaneous multiple selective targeting using antibody-conjugated gold nanorods," Opt. Express **16**(23), 18605–18615 (2008).
19. S. Mallidi, T. Larson, J. Tam, P. P. Joshi, A. Karpiouk, K. Sokolov, and S. Emelianov, "Multiwavelength Photoacoustic Imaging and Plasmon Resonance Coupling of Gold Nanoparticles for Selective Detection of Cancer," Nano Lett. **9**(8), 2825–2831 (2009).
20. M. H. Xu and L. H. V. Wang, "Photoacoustic imaging in biomedicine," Rev. Sci. Instrum. **77**(4), 041101 (2006).
21. M. C. Pierce, R. A. Schwarz, V. S. Bhattar, S. Mondrik, M. D. Williams, J. J. Lee, R. Richards-Kortum, and A. M. Gillenwater, "Accuracy of in vivo multimodal optical imaging for detection of oral neoplasia," Cancer Prev. Res. (Phila.) **5**(6), 801–809 (2012).
22. J. D. Meier, H. Xie, Y. Sun, Y. Sun, N. Hatami, B. Poirier, L. Marcu, and D. G. Farwell, "Time-resolved laser-induced fluorescence spectroscopy as a diagnostic instrument in head and neck carcinoma," Otolaryngol. Head Neck Surg. **142**(6), 838–844 (2010).
23. Y. Sun, J. Phipps, D. S. Elson, H. Stoy, S. Tinling, J. Meier, B. Poirier, F. S. Chuang, D. G. Farwell, and L. Marcu, "Fluorescence lifetime imaging microscopy: in vivo application to diagnosis of oral carcinoma," Opt. Lett. **34**(13), 2081–2083 (2009).
24. D. G. Farwell, J. D. Meier, J. Park, Y. Sun, H. Coffman, B. Poirier, J. Phipps, S. Tinling, D. J. Enepekides, and L. Marcu, "Time-Resolved Fluorescence Spectroscopy as a Diagnostic Technique of Oral Carcinoma: Validation in the Hamster Buccal Pouch Model," Arch. Otolaryngol. Head Neck Surg. **136**(2), 126–133 (2010).
25. M. C. Skala, K. M. Riching, A. Gendron-Fitzpatrick, J. Eickhoff, K. W. Eliceiri, J. G. White, and N. Ramanujam, "In vivo multiphoton microscopy of NADH and FAD redox states, fluorescence lifetimes, and cellular morphology in precancerous epithelia," Proc. Natl. Acad. Sci. U.S.A. **104**(49), 19494–19499 (2007).
26. J. A. Jo, B. E. Applegate, J. Park, S. Shrestha, P. Pande, I. B. Gimenez-Conti, and J. L. Brandon, "In vivo simultaneous morphological and biochemical optical imaging of oral epithelial cancer," IEEE. T Biomed. Eng. (N.Y.) **57**, 2596–2599 (2010).
27. R. H. Spiro, A. G. Huvos, G. Y. Wong, J. D. Spiro, C. A. Gnecco, and E. W. Strong, "Predictive value of tumor thickness in squamous carcinoma confined to the tongue and floor of the mouth," Am. J. Surg. **152**(4), 345–350 (1986).
28. S. H. Huang, D. Hwang, G. Lockwood, D. P. Goldstein, and B. O'Sullivan, "Predictive value of tumor thickness for cervical lymph-node involvement in squamous cell carcinoma of the oral cavity: a meta-analysis of reported studies," Cancer **115**(7), 1489–1497 (2009).
29. F. L. Lizzi, M. Greenebaum, E. J. Feleppa, M. Elbaum, and D. J. Coleman, "Theoretical framework for spectrum analysis in ultrasonic tissue characterization," J. Acoust. Soc. Am. **73**(4), 1366–1373 (1983).
30. I. B. Gimenez-Conti and T. J. Slaga, "The Hamster Cheek Pouch Carcinogenesis Model," J. Cell. Biochem. Suppl. **17F**(S17F), 83–90 (1993).
31. J. J. Salley, "Experimental Carcinogenesis in the Cheek Pouch of the Syrian Hamster," J. Dent. Res. **33**(2), 253–262 (1954).
32. Y. H. Sun, Y. Sun, D. Stephens, H. T. Xie, J. Phipps, R. Saroufeem, J. Southard, D. S. Elson, and L. Marcu, "Dynamic tissue analysis using time- and wavelength-resolved fluorescence spectroscopy for atherosclerosis diagnosis," Opt. Express **19**(5), 3890–3901 (2011).
33. Y. Sun, R. Liu, D. S. Elson, C. W. Hollars, J. A. Jo, J. Park, Y. Sun, and L. Marcu, "Simultaneous time- and wavelength-resolved fluorescence spectroscopy for near real-time tissue diagnosis," Opt. Lett. **33**(6), 630–632 (2008).
34. J. Liu, Y. Sun, J. Qi, and L. Marcu, "A novel method for fast and robust estimation of fluorescence decay dynamics using constrained least-squares deconvolution with Laguerre expansion," Phys. Med. Biol. **57**(4), 843–865 (2012).
35. K. C. B. Lee, J. Siegel, S. E. D. Webb, S. Lévêque-Fort, M. J. Cole, R. Jones, K. Dowling, M. J. Lever, and P. M. W. French, "Application of the Stretched Exponential Function to Fluorescence Lifetime Imaging," Biophys. J. **81**(3), 1265–1274 (2001).

#193145 - $15.00 USD Received 1 Jul 2013; revised 9 Aug 2013; accepted 9 Aug 2013; published 26 Aug 2013

36. M. Y. Berezin and S. Achilefu, "Fluorescence lifetime measurements and biological imaging," Chem. Rev. **110**(5), 2641–2684 (2010).
37. K. Sokolov, J. Galvan, A. Myakov, A. Lacy, R. Lotan, and R. Richards-Kortum, "Realistic three-dimensional epithelial tissue phantoms for biomedical optics," J. Biomed. Opt. **7**(1), 148–156 (2002).
38. M. A. Hollingsworth and B. J. Swanson, "Mucins in cancer: protection and control of the cell surface," Nat. Rev. Cancer **4**(1), 45–60 (2004).
39. V. P. Bhavanandan, N. J. Ringler, and D. C. Gowda, "Identification of the glycosidically bound sialic acid in mucin glycoproteins that reacts as "free sialic acid" in the Warren assay," Glycobiology **8**(11), 1077–1086 (1998).
40. I. K. Cohen, C. W. Moncure, R. J. Witorsch, and R. F. Diegelmann, "Collagen Synthesis in Capsules Surrounding Dimethylbenzanthracene-induced Rat Breast Tumors and the Effect of Pretreatment with β-Aminopropionitrile," Cancer Res. **39**(8), 2923–2927 (1979).
41. V. Lutz, M. Sattler, S. Gallinat, H. Wenck, R. Poertner, and F. Fischer, "Impact of collagen crosslinking on the second harmonic generation signal and the fluorescence lifetime of collagen autofluorescence," Skin Res. Technol. **18**(2), 168–179 (2012).

1. Introduction

Cancer is the second leading cause of death in the United States with a total of 1,660,290 new cancer cases and 580,350 cancer deaths projected in 2013 [1]. The diagnosis and prognosis of cancer involves studying multiple features pertaining to structure, function and biochemistry of tissue. The need for evaluating these features *in vivo* for rapid diagnostics has led to development of numerous imaging techniques with ongoing focus on multimodal imaging technology. Multimodal imaging is widely considered to employ two or more imaging techniques in a single examination to allow acquisition of co-registered complementary data from tissue. For example, a variety of multimodal imaging systems are clinically available or under research investigation that involve combination of either positron emission tomography (PET), X-ray computed tomography (CT), magnetic resonance (MR), single photon emission counting tomography (SPECT) or ultrasound [2]. More recently, optical techniques have also been employed to develop multimodal systems for *in vivo* imaging, including combination of time-resolved fluorescence spectroscopy and ultrasound [3], optical coherence tomography (OCT) and fluorescence imaging [4], fluorescence and MRI [5], and fluorescence intravital microscopy, dynamic light scattering and spectrally enhanced microscopy [6]. Optical imaging techniques provide biochemical and/or functional information with high sensitivity that can be complemented with depth dependent structural information from other modalities (such as ultrasound) which is otherwise not available due to limited penetration of light in tissue. Such multimodal techniques provide a means for rapid cancer diagnosis by providing holistic information about tissue pathology.

Many factors affect the long-term prognosis of patient suffering from cancer, including pathology, location of the cancer, stage of disease, histologic grade, and for some cancers the biologic and genetic properties of the cancer cells (biomarkers). Oral cancer, for example, is identified either by direct visualization, manual palpation or via radiologic analysis. The diagnosis is then confirmed with tissue sampling and histology analysis with either a fine needle aspiration or an incisional/excisional biopsy. Once the diagnosis is secured, treatment typically involves surgery, radiation, chemotherapy or any combination thereof, depending on the pathology of the cancer, location and stage at the time of diagnosis. Detection of cancer at an early stage not only allows for treatment with decreased morbidity, but also improves patient quality of life post-treatment. The 5-year survival rates greatly improve if a cancer is diagnosed at an early stage. For instance, 5-year survival rate of the oral cancer is 82% for stage I, but precipitously drops off to only 35% for stage IV disease [7]. Hence, non-invasive diagnostic techniques that can delineate cancerous tissue at an early stage will prove extremely beneficial for patients. In order to detect cancer, one can probe in to structural and biochemical changes in tissue.

The most common technique for imaging and diagnosing oral cancer in humans includes white light endoscopy followed by histopathology examination of biopsy specimens. Alternative non-invasive techniques that are used or are under research investigation include

#193145 - $15.00 USD Received 1 Jul 2013; revised 9 Aug 2013; accepted 9 Aug 2013; published 26 Aug 2013

radiography, CT [8, 9], low-frequency ultrasound [10], MRI [11] and PET [8, 12, 13]. Optical imaging techniques that are under investigation include autofluorescence based imaging [14], surface enhanced Raman spectroscopy imaging [15], OCT [16, 17] and photoacoustic imaging [18–20]. While these techniques provide valuable diagnostic information from tissue, multimodal imaging methods provide more superior results for oral cancer diagnosis as demonstrated by Pierce et al. [21].

This study investigates the ability of a multimodal technique for synergistic characterization and diagnosis of carcinomas. *In vivo* multimodal imaging of oral cancer was performed in a hamster model using a prototype device that integrates three imaging techniques namely: 1) fluorescence lifetime imaging (FLIm), which is sensitive to biochemical changes on tissue surface; 2) ultrasound backscatter microscopy (UBM), that allows evaluation of tissue microstructure and morphology; and 3) photoacoustic imaging (PAI), which is sensitive to changes in tissue vascularization. FLIm unlike fluorescence intensity measurements, takes in to account the characteristics of fluorescence decay dynamics (excited state lifetime) of the fluorophore. In oral carcinoma, FLIm is anticipated to differentiate between normal and cancerous tissue based on differences in fluorescence signatures owing to changes in collagen content and bound/unbound states of nicotineamide adenine dinucleotide (NADH) in tissue [22–26]. High-frequency UBM has the potential to provide information on microstructure and thickness of underlying tissue that is known to be important for oral cancer diagnostics [27, 28]. In addition, quantitative analysis of ultrasound radio-frequency (RF) data allows characterization of tissue condition [29]. PAI can enable imaging of blood vessels and may help in detecting tumor regions that are often more vascularized than normal tissue. The presented work evaluates for the first time whether complementary diagnostic features can be measured via a compact multimodal scanning probe that allows for direct co-registration of biochemical, structural, and functional characteristics of tissue *in vivo*.

2. Methods

2.1 Animal care and intervention protocol

The hamster buccal pouch model used in this study is a well described and accepted technique of oral carcinogenesis for *in vivo* tissue analysis [30, 31]. This model permits the study of cancer progression (from normal, to dysplasia, to carcinoma in situ or invasive carcinoma) via repeated exposure of the buccal mucosa to a carcinogen.

Twenty-four male, golden/Syrian hamsters, 5 to 6 weeks of age, were obtained from Charles River Laboratories (Wilmington, Massachusetts). The experimental procedure was approved by the Institution for Animal Care and Use Committee at the University of California, Davis, to ensure acceptable humane treatment of the hamsters and the approved protocol was strictly followed.

The right and left buccal pouch of 14 hamsters were topically painted with 0.5% 7, 12-Dimethylbenz(a)anthracene (DMBA) solution dissolved in mineral oil 3 times a week to induce lesion formation. The 14 hamsters were divided in to two equal groups with different DMBA treatment durations representing pre-cancer (6 week treatment) and invasive carcinoma (16 week treatment). In addition, 10 hamsters were not exposed to DMBA solution and were treated as a healthy control group. At the end of the treatment duration, the respective animals were anesthetized with 200 mg⁄kg ketamine and 13 mg⁄kg xylazine. The region of interest (ROI) for imaging was identified via visual inspection by an otolaryngologist. The cheek pouch was reverted to expose the ROI with a customized brace (Fig. 1(b)) and measurements were performed using the multi-modal probe perpendicular to the tissue surface. For UBM imaging, a small petri dish with its bottom cut out over the ROI was gently fastened over the cheek and filled with phosphate buffered saline (PBS) to provide an acoustic coupling medium. Petroleum jelly (Vaseline, Unilever) was used on sides to

#193145 - $15.00 USD Received 1 Jul 2013; revised 9 Aug 2013; accepted 9 Aug 2013; published 26 Aug 2013

prevent leakage. The UBM image was also used to generate a surface profile that allowed changing the probe height accordingly to maintain a fixed working distance (4 mm for PAI and 1 mm for FLIm) over an irregular surface. The animal and tissue ROI were photographed before measurements and tissue ink was used to mark the direction of imaging to allow spatial correlation with histology. Following data acquisition, the animal was sacrificed, and tissue within the ROI was excised for pathological examination.

2.2 Instrumentation and data acquisition

2.2.1 Multimodal system configuration

The schematic diagram of the multimodal system combining FLIm, PAI and UBM subsystems is shown in Fig. 1. The multimodal tissue interrogation probe enabling the integration of three modalities consists of a ring ultrasonic transducer shared by the UBM and PAI sub-systems, an optical fiber which serves as excitation-collection pathway in the FLIm subsystem, and a ring of 16 optical fibers which serve as excitation pathway in the PAI subsystem.

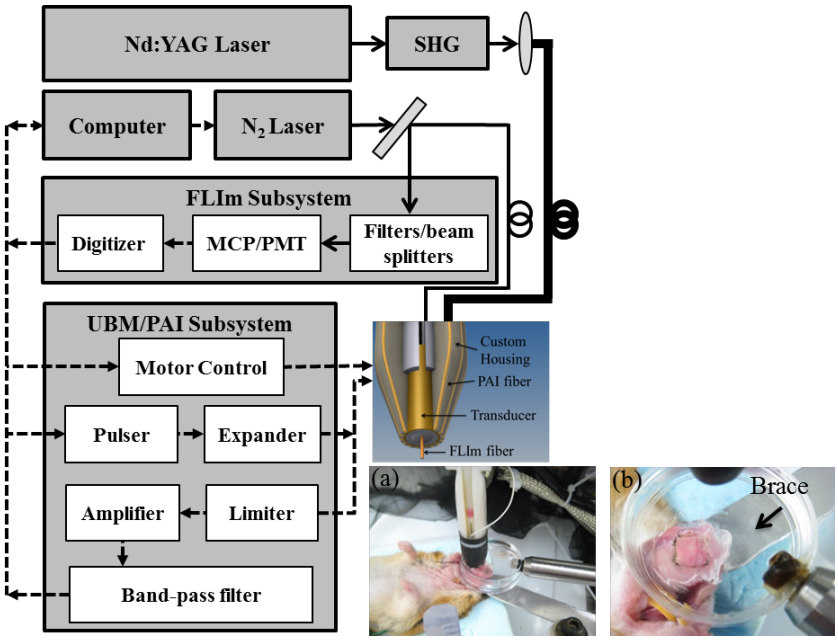

Fig. 1. Schematic of the hybrid multimodal scanning FLIm, UBM and PAI system. The system consists of laser source(s), computer unit, FLIm subsystem, UBM/PAI subsystem and the multimodal scanning probe housing the ultrasound transducer, FLIm optical fiber and PAI fibers. Bottom right: (a) picture of the multimodal probe positioned above the hamster cheek pouch, and (b) magnified view of brace and petri-dish over reverted cheek pouch.

All probe elements are fit into a custom built housing manufactured using a 3-D printer (Eden 260V, Objet Ltd., Rehovot, Israel). The FLIm optical fiber passes through a central circular aperture of radius 0.9 mm in the ultrasonic transducer. The PAI fibers are located in a concentric ring and oriented at an angle (19°) with respect to the vertical axis such that the resulting beam converges at 4 mm from the fiber tip. The FLIm fiber can protrude out of the probe to allow adjustment of the probe working distance down to 1 mm. The multimodal probe was mounted on a XYZ-linear positioning stage (1 μm resolution, Parker Hannifin Corp., USA) to allow scanning of the tissue ROI and obtain 2-D FLIm, and 3-D UBM/PAI images.

#193145 - $15.00 USD Received 1 Jul 2013; revised 9 Aug 2013; accepted 9 Aug 2013; published 26 Aug 2013

2.2.2 FLIm subsystem

A fast multispectral and scanning time-resolved fluorescence spectroscopy technique [32, 33] was used to obtain FLIm data from the tissue ROI with a spatial resolution smaller than 0.2 mm. Briefly, the system is comprised of a pulsed nitrogen laser source (337 nm, 800 ps pulse width, 30 Hz repetition rate) coupled to a 600 µm core UV-grade silica/silica optical fiber (FVP400440480, Polymicro, Phoenix, AZ). The energy delivered to tissue was maintained at 2 µJ/pulse (fluence - 0.16 mJ/cm^2 from a 600 µm core fiber) which is well below the permissible ANSI UV exposure limit for biological tissue (3 mJ/cm^2). The fluorescence emission was collected using the same fiber. Fluorescence light was spectrally resolved into four wavelength subbands (channels) using a series of 45° dichroic beam splitters and band-pass filters (Semrock, Rochester, NY). The fluorescence subbands have a central wavelength/bandwidth of 390/40 nm (channel 1, CH1), 450/45 nm (channel 2, CH2), 542/50 nm (channel 3, CH3), and 629/53 nm (channel 4, CH4) respectively. The signal was then coupled into four fibers with varying lengths of 1, 10, 19 and 28 m to introduce time delays between the subband signals. The proximal ends of the fibers are coupled to a multichannel plate photomultiplier (MCP-PMT) with a 180 ps rise time (R5916U-50, Hamamatsu, Bridgewater, NJ). The electronic signals from the MCP-PMT are amplified by a preamplifier (1.5 GHz bandwidth, Hamamatsu, Japan) and recorded by a digital oscilloscope (DPO7254, 2.5 GHz bandwidth, 20 GHz sampling rate, Tektronix Inc., Richardson, TX).

2.2.3 UBM subsystem

A customized 41-MHz press focused ultrasonic transducer (Ultrasonic Transducer Resource Center, University of Southern California) with a focal depth of 6 mm, 70% bandwidth and 3 mm diameter and a central circular aperture of diameter 0.9 mm was employed for UBM imaging and detecting PAI signal. The scanning provided a spatial resolution of smaller than 0.1 mm and depth sensitivity of at least 4 mm.

A high-voltage pulser (AVB2-TE-C, Avtech Electrosystems Ltd.) generating a wideband short pulse at 41 MHz was used to drive the UBM transducer. The receiving circuit in addition to the transducer included an expander (custom built) to prevent the noise from the pulser from contaminating the signal. A limiter (custom built) was also used to protect the receiving circuit. Backscattered ultrasound waves were detected by the transducer, amplified with a low noise amplifier (Miteq 1114, MITEQ) by 35 dB, and recorded by a digitizer (CompuScope 12400, Gage Applied Technologies) with a sampling rate of 400 MHz.

2.2.4 PAI subsystem

The PAI subsystem shared the same transducer and the receiving circuit as described in the UBM subsystem to acquire and digitize the PAI signals. PAI illumination was achieved using a frequency doubled excitation laser (CFR200 Nd:YAG, 10 ns pulse width, 1-20 Hz variable repetition rate, max pulse energy 200 mJ, Big Sky Corporation Bozeman, MT) using 16 polymethyl-methacrylate (PMMA) optical fibers (480 µm core diameter each, SK20, Mitsubishi Rayon Co., Tokyo, Japan) arranged in a concentric ring with a 19° tilt angle from the vertical axis. The excitation light (532 nm) was coupled into the PAI fibers by first focusing the laser beam in to 600 µm core UV grade silica/silica fiber positioned at a 6° angle with respect to the laser beam. This ensured that light was coupled into only the higher modes of the fiber, creating a diverging ring or “donut shaped” beam on the distal side of the silica fiber. This beam was then coupled into the proximal section of the PAI illumination fiber bundle. The photo-acoustic signal generated from the illuminated tissue ROI was collected using the UBM transducer.

#193145 - $15.00 USD Received 1 Jul 2013; revised 9 Aug 2013; accepted 9 Aug 2013; published 26 Aug 2013

2.2.5 Data acquisition

Co-registered FLIm, PAI and UBM data was acquired sequentially from the tissue ROI by raster scanning. Initially, a fast UBM scan was performed to obtain the surface profile of the ROI to allow adjusting the height of the probe during the acquisition to maintain a fixed working distance from tissue for FLIm and PAI. Scanning was performed over an area of 3 x 3 mm^2 or 5 x 5 mm^2. The scan area was reduced for some animals to reduce acquisition time when it was expected that the animal was nearing death which was determined with the onset of lower breathing rate as monitored by the otolaryngology resident present during the imaging procedure. 3-D UBM scanning was performed with an axial (x) and lateral (y) pixel sizes of 0.02 mm and 0.1 mm respectively. The transducer was driven with a voltage of 60 V_{pp} with a pulse repetition frequency of 500 Hz and data acquisition rate of 400 MHz. Each A-line scan along the depth (z) comprised of 5120 samples equivalent to a depth of 9.6 mm. The axial (x) scan speed was set to 1.25 mm/s and samples were averaged eight times to improve SNR. The intensity versus depth sensitivity curve was obtained by recording pulse-echo signal from a metal reflector placed at different depths from the transducer. This curve was used to correct for depth dependent intensity variations in the focal region of the transducer. PAI raster-scanning and acquisition was performed similar to UBM. The laser pulse rate was set to 20 Hz and the delivered energy was approximately 19 mJ/cm^2 (ANSI limit – 20 mJ/cm^2). Each PAI A-line scan had 2432 samples along depth (z) corresponding to 9.14 mm. The PAI scanning speed in the x-direction was 0.2 mm/s with lateral and axial pixel sizes of 0.02 mm and 0.2 mm respectively. FLIm raster scanning was performed using a 600 µm core UV-grade silica/silica optical fiber with a working distance of 1 mm. Data was acquired at 8 GHz with laser repetition rate of 30 Hz and 16 samples per average. The axial and lateral pixel sizes for FLIm were 0.1 mm and 0.2 mm respectively.

2.2.6 Data co-registration

Sequential FLIm, UBM and PAI measurements allowed near perfect co-registration between the different modalities without the use of fiducial markers as they share the same imaging axis. The speed of data acquisition was different between different modalities due to difference in laser repetition rates (PAI – 20 Hz, FLIm – 30 Hz). Co-registration with histology was achieved by marking the imaged ROI with ink. Additionally, the ROI was also labeled to identify the XY- direction of the raster scan.

2.3 Histological preparation and analysis

Excised tissue samples were preserved in 10% buffered formalin. The specimens were embedded in paraffin and sectioned for hematoxylin and eosin (H&E) to observe general pathology features and morphology, and Masson's trichrome staining to observe collagen and muscle fiber content. Histologic sections were analyzed by a board certified anatomic pathologist, who was blind to the imaging results.

2.4 Data analysis

2.4.1 FLIm data processing

The measured fluorescence decay intensity at each point on the tissue ROI is defined as $y(t)$ which is a convolution of the actual fluorescence decay $h(t)$ and the instrument impulse response $I(t)$. In discrete time, for N equal sampling time points $t_i = i\delta t$, $i = 0.....,N-1$ and sampling interval δt gives,

$$y(k) = \sum_{i=0}^{k} I(k-i) \cdot h(i), \qquad (1)$$

#193145 - $15.00 USD Received 1 Jul 2013; revised 9 Aug 2013; accepted 9 Aug 2013; published 26 Aug 2013

where $k = 0,\ldots,N-1$. $h(k)$ was expanded on to a set of discrete ordered Laguerre basis functions, b_l such that,

$$h(k) = \sum_{l=0}^{L-1} c_l b_l(k;\alpha), \tag{2}$$

where L and α are the basis parameters and c_l is the l^{th} expansion coefficient. $h(k)$ was determined using a fast constrained least square deconvolution technique [34]. This technique, unlike multi-exponential models does not involve a non-linear optimization scheme with a non-unique solution and eliminates the need for *a priori* knowledge of the number of decay components that can be arbitrary for a complex fluorophore system such as tissue [35]. Additionally, the method provides a faster way of computing lifetimes that would be important in a clinical setting. The average lifetime was calculated as,

$$\tau_{avg} = \frac{\delta t \sum_k k h(k)}{\sum_k h(k)}. \tag{3}$$

As a result, for every point on the tissue ROI, the absolute fluorescence intensity, fluorescence lifetime and Laguerre expansion coefficients were computed to generate a 2-D FLIm, intensity and Laguerre coefficient map. The fluorescence intensity was computed as the numerical integration of the decay curve for each wavelength sub-band. In this study, time-resolved results from CH1and CH2 are reported pertaining to fluorescence from collagen and NADH respectively. Measurements from CH3 and CH4 are not reported owing to low signal to noise ratio because there are no biomolecules fluorescing in these bands for the tissue being imaged. A 12th order Laguerre expansion was implemented and the 2nd order Laguerre coefficient values (LC-1) were used to generate the 2-D Laguerre coefficient maps. This coefficient describes the slow component of the fluorescence decay dynamics and it was expected to show contrast when the measured fluorescence signal varied from being predominantly from collagen to predominantly from NADH as tumor develops in tissue.

2.4.2 UBM/PAI data processing

The UBM and PAI radio frequency data were reconstructed to form a 2-D image by displaying the log compressed amplitude of the Hilbert transform of the scanning A-line data. DC offset was subtracted from the data and a band pass filter (25-60 MHz) was employed for noise reduction. UBM, PAI and FLIm images are co-registered as they share the same imaging z-axis. UBM images were studied for structural information and PAI images for both structure and vasculature and correlated with results from FLIm and validated with histology.

The UBM raw RF data were also used to compute the backscatter coefficient function $B_c(f)$, integrated backscatter coefficients (IB) and the energy norm (E) from imaged regions of interests to quantify changes in UBM results observed between different tissue conditions (normal, pre-cancer and carcinoma). RF data from randomly selected regions of interest for each tissue condition confirmed from histology was used to compute the aforementioned parameters.

$B_c(f)$ for the sample was computed by correcting for the system response by normalizing the sample surface spectra with the reference spectra:

$$B_c(f) = \frac{S_S(z,f)}{S_R(z,f)}, \tag{4}$$

where $S_S(z,f)$ and $S_R(z,f)$ are the frequency f and depth (z) dependent spectra obtained from the segment of the ultrasound signal representing the sample–liquid interface and

#193145 - $15.00 USD Received 1 Jul 2013; revised 9 Aug 2013; accepted 9 Aug 2013; published 26 Aug 2013

reflector-liquid interface respectively. Both spectra are estimated by calculating the Fast Fourier Transform (FFT) of the Hamming windowed segments of the corresponding backscattered signal. The IB value was computed from the backscatter coefficient function in dB, $B_c^{dB}(f)$, over the bandwidth Δf of $S_R(z, f)$:

$$B_c^{dB} = 10\log_{10}\left\langle \left| B_c(f) \right|^2 \right\rangle, \tag{5}$$

$$IB = \frac{1}{\Delta f}\int_{\Delta f} B_c^{dB}(f)df. \tag{6}$$

The energy norm (E) of a given region of interest is defined as:

$$E = \sqrt{v.v^T}. \tag{7}$$

where v are the Hamming windowed segments of the corresponding backscattered RF signal. The energy norm depicts the amount of absolute ultrasound energy backscattered from a sample.

3. Results

This paper presents results from representative tissue conditions to demonstrate the ability of the multimodal system to evaluate pathological features of oral carcinoma. Three different tissue conditions were observed and analyzed: 1) control/normal, 2) pre-cancer and 3) invasive carcinoma with successful co-registered results from 5, 3 and 4 animals respectively. Thirteen animals expired before or during imaging and results from these animals are not reported here. Representative results from each condition are shown in Figs. 2, 3, and 4. In addition, a few case studies that show the capability of the multimodal technique to visualize particular features (e.g. loss of layered structure and mucin accumulation) are presented that can aid in diagnosis of cancer (Figs. 5 and 6). Figures 7 and 8 summarize quantitative FLIm and UBM results from different tissue conditions for comparative analysis.

3.1 Characterization of normal tissue

Representative results from FLIm, UBM and PAI measurements and the corresponding histology analysis from normal hamster cheek epithelial tissue are depicted in Fig. 2. The picture of the imaged region on the hamster cheek (Fig. 2(h)) shows a uniform area with no visual abnormalities. For this case, the FLIm and PAI imaged region was smaller than the UBM imaged region and is marked by the blue bounding box (Fig. 2(h)). Fluorescence intensity (Fig. 2(a)) showed variability across the surface, while the time-resolved data (Figs. 2(b)-2(c)) yielded uniform lifetime and LC-1 values across the imaged area. The mean average lifetime values were 5.1 ± 0.2 ns and 4.8 ± 0.2 ns from CH1 and CH2 respectively (Figs. 2(f) and 2(g)) indicating a small intra-sample lifetime variability. The lifetime values resemble those of collagen (5-6 ns) [36] which is the predominant fluorophore in most tissue types [37] as confirmed from histology (Figs. 2(i) and 2(j)). The contribution of NADH fluorescence in CH2, however, lowers the lifetime to the observed value. LC-1 values that describe the slow decay component of the measured fluorescence were - 0.03 ± 0.01. Since lifetime is independent of intensity, FLIm images are more consistent and indicative of the tissue condition than absolute intensity values which appear to show variation (Fig. 2(a)). The histology cross-section (Figs. 2(i) and 2(j) along the back dotted line in Fig. 2(h)) confirmed normal tissue pathology with distinct epithelium and sub-epithelium connective tissue (E), muscle fiber mucosa (M) and adventitial connective tissue (A). This organized layered structure was observed on corresponding UBM cross sectional scan (Fig. 2(d)). Hyperechoic layer is seen at the bottom region and is attributed to the back of the cheek pouch. Corresponding PAI cross sectional image showed high signal intensity (Fig. 2(e)) that appears

#193145 - $15.00 USD Received 1 Jul 2013; revised 9 Aug 2013; accepted 9 Aug 2013; published 26 Aug 2013

to arise from blood vessels in the muscularis as seen in H&E histology (Fig. 2(j), black arrows labeled C and D).

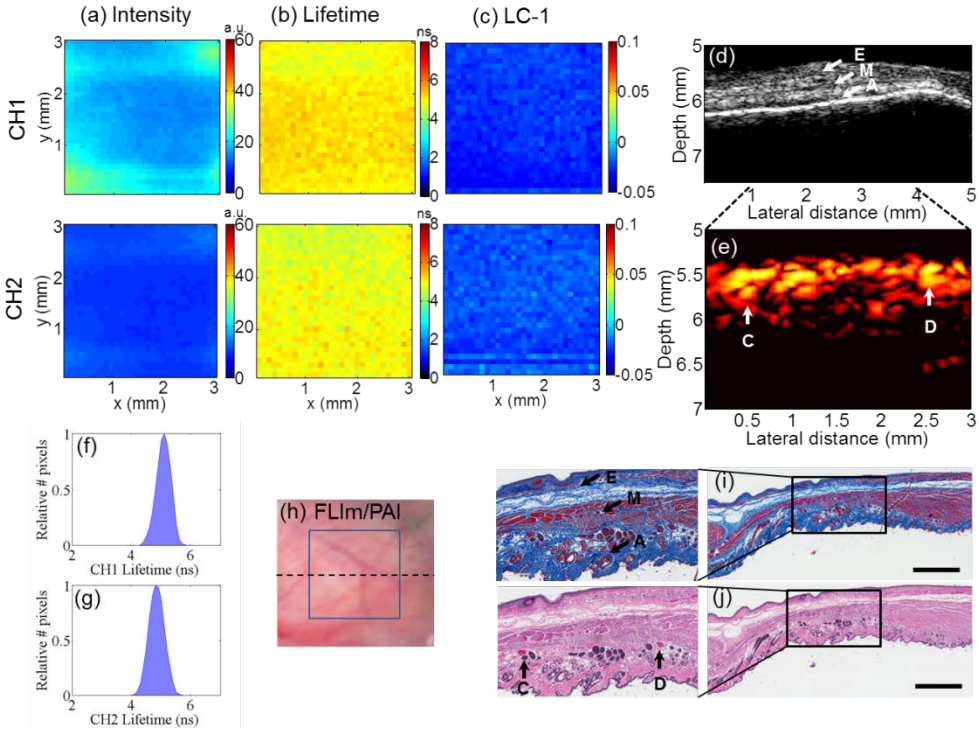

Fig. 2. Normal hamster cheek tissue. FLIm images showing (a) intensity map, (b) average lifetime map, and (c) LC-1 map from two wavelength bands CH1 (390/40 nm) (top) and CH2 (450/45 nm) (bottom); (d) UBM B-mode image and (e) PAI B-mode image; (f) CH1 and (g) CH2 lifetime histogram over the entire imaged region; (h) Picture of hamster cheek with FLIm and PAI imaging region (blue box); (i) Masson's Trichrome and (j) H&E histological section taken from the black dotted line in (h) and co-registered with UBM and PAI image. Magnified histology image is shown left to (i) and (j) corresponding to the region enclosed by black boxes. Black arrows in magnified trichrome section point to the different layers seen in tissue: E – Epithelium and sub-epithelium connective tissue, M – muscle fiber mucosa, A – adventitial connective tissue which can also be seen in the UBM image. The high intensity signal in the UBM image at the bottom is due to high reflection of ultrasound from the back of the cheek. High PAI signal intensity is seen in regions (white arrows, C, D) that correspond to blood vessels identified in histology (magnified H&E section, arrows C and D). Scale bars are 1 mm.

3.2 Characterization of precancerous tissue

Representative results from FLIm, UBM and PAI measurements and the corresponding histology analysis from hamster cheek epithelial tissue showing an early lesion (precancer) are shown in Fig. 3.

#193145 - $15.00 USD Received 1 Jul 2013; revised 9 Aug 2013; accepted 9 Aug 2013; published 26 Aug 2013

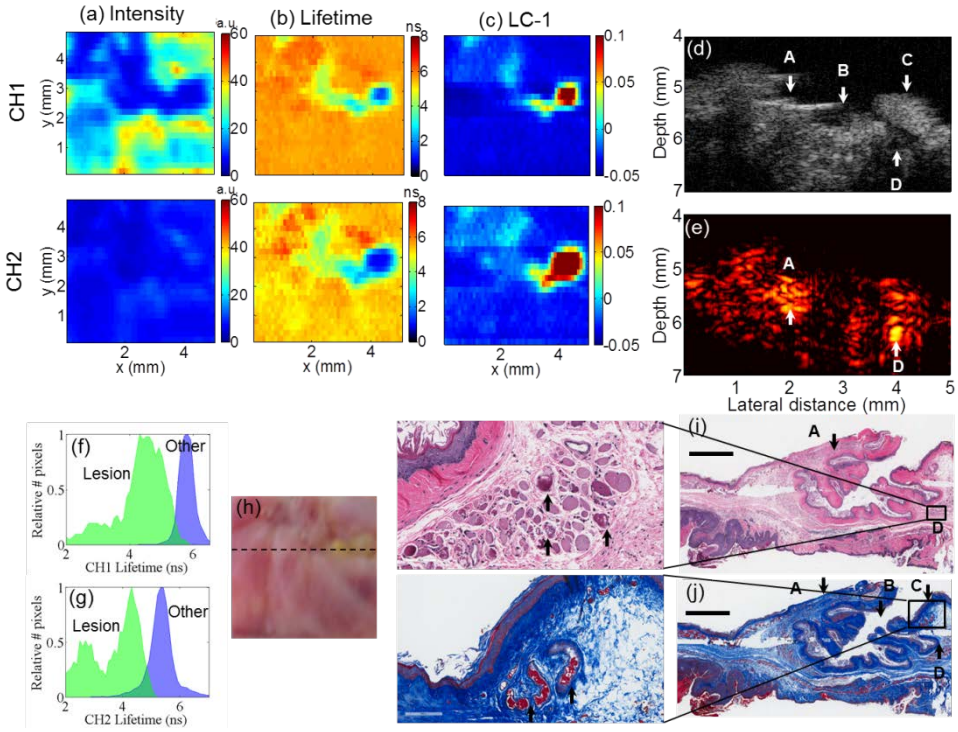

Fig. 3. Hamster cheek tissue from precancer group. FLIm images showing fluorescence (a) intensity map, (b) average lifetime map, and (c) LC-1 map from two wavelength bands CH1 (390/40 nm) (top) and CH2 (450/45 nm) (bottom); (d) UBM B-mode image and (e) PAI B-mode image; (f) CH1 and (g) CH2 lifetime histogram showing two distinct lifetime distributions. (h) Picture of hamster cheek; (i) Masson's Trichrome and (j) H&E histological section taken from the black dotted line in (h) and co-registered with UBM and PAI image. Magnified histology image is shown left to (i) and (j) corresponding to the region enclosed by black boxes. Black arrows in (j) Trichrome section point to A – collagen with muscle fibers, B – pulsatile diverticulum, C – lesion, D – collagen layers with blood vessels which can also be observed in UBM image with varying echogenicities. High PAI signal intensity is seen in regions (white arrows A and D, (e)) that correspond to blood vessels identified in histology (magnified H&E and trichrome section). Scale bars are 1 mm.

The picture of the imaged region (Fig. 3(h)) shows tissue with abnormality in the upper right (yellow brown discoloration) which was confirmed to be precancer from histology (Figs. 3(i) and 3(j), arrow C on trichrome section). No distinctive features were observed in the intensity image (Fig. 3(a)) in contrast with the time-resolved images (Figs. 3(b)-3(c)) which provided a clear delineation of the area with abnormal appearance. This area has a lower lifetime (CH1, 4.2 ± 0.9 ns, CH2, 3.2 ± 1.2 ns) when compared with the surrounding area with normal appearance (CH1, 5.8 ± 0.2 ns, CH2, 5.3 ± 0.5 ns) (Figs. 3(f) and 3(g)). Figures 3(i) and 3(j) show a histological section taken along the black dotted line (Fig. 3(h)) confirming the presence of precancer with thickening of epithelium (at C) and vascularization (magnified trichrome section). Note that not all animals in this group showed distinct abnormal features in histology. However, all cases in this group showed regions with increased collagen content (confirmed from histology) when compared with tissue from normal cases. FLIm results from these collagen-rich regions demonstrated consistently higher average lifetime values (both from CH1 and CH2) compared to results from the normal group.

UBM cross sectional scan (Fig. 3(d)) showed varying echogenecities from the different features identified in histology (trichrome section). Blood vessels were also identified in the H&E section (black arrows, A and D) that show higher signal intensity in the PAI cross

#193145 - $15.00 USD Received 1 Jul 2013; revised 9 Aug 2013; accepted 9 Aug 2013; published 26 Aug 2013

sectional scan (Fig. 3(e), arrows A and D). Vasculature in histology appears smaller than what would actually be present due to shrinkage after histological processing.

3.3 Characterization of invasive carcinoma tissue

Representative results from FLIm, UBM and PAI measurements and the corresponding histology analysis from hamster cheek epithelial tissue showing invasive carcinoma are presented in Fig. 4.

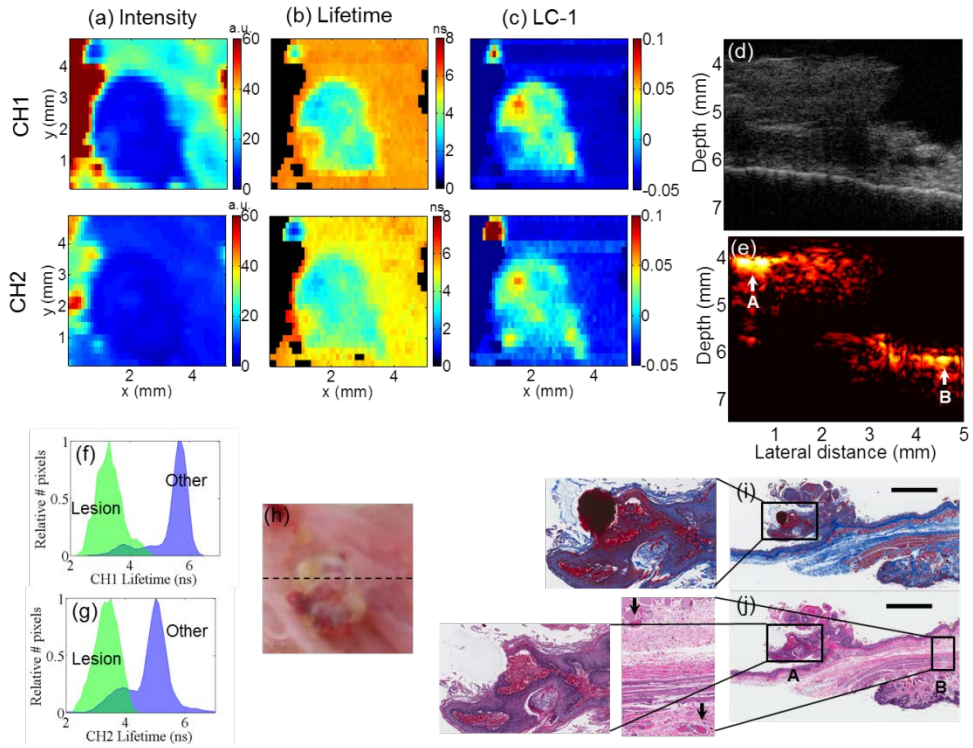

Fig. 4. Hamster cheek tissue from carcinoma group. FLIm images showing fluorescence (a) intensity map, (b) average lifetime map, and (c) LC-1 map from two wavelength bands CH1 (390/40 nm) (top) and CH2 (450/45 nm) (bottom); (d) UBM B-mode image and (e) PAI B-mode image; (f) CH1 and (g) CH2 lifetime histogram showing two distinct lifetime distributions. (h) Picture of hamster cheek; (i) Masson's Trichrome and (j) H&E histological section taken from the black dotted line cross-section in (h) and co-registered with UBM and PAI image. Magnified histology image is shown left to (i) and (j) corresponding to the region enclosed by black boxes. Histology sections show disruption of tissue structure which is seen in the UBM image as hypoechoic regions. Black arrows (magnified H&E section, A and B) show vascularization and large blood accumulation in the tumor region. High PAI signal intensity is seen in regions (white arrows A and B, (e)) that correspond to vascularization and blood accumulation identified in histology. Scale bars are 1 mm.

The imaged region on the hamster cheek (Fig. 4(h)) shows a large non-uniform abnormality in the center which is confirmed to be invasive carcinoma from histology (Figs. 4(i) and 4(j)). Both fluorescence intensity and time-resolved images (Figs. 4(a)-4(c)) show clear delineation of the abnormal region. The carcinoma region showed low fluorescence intensity in both wavelength bands (Fig. 4(a)) and a lower lifetime (CH1, 3.5 ± 0.5 ns, CH2, 3.5 ± 0.4 ns) when compared with the surrounding tissue (CH1, 4.6 ± 2.1 ns, CH2, 4.0 ± 2.0 ns) (Figs. 4(f) and 4(g)). Note that the left portion of the intensity image has an artifact that resulted from fluorescence emission from Vaseline gel that was used to seal the sides of the petri-dish filled with PBS during UBM measurements. The high lifetime region from Vaseline

#193145 - $15.00 USD Received 1 Jul 2013; revised 9 Aug 2013; accepted 9 Aug 2013; published 26 Aug 2013

was blacked out in the lifetime images. LC-1 values of the tumor region had positive values when compared to the normal regions which were always less than zero. Figures 4(i) and 4(j) show a sample histological section taken from the region represented by the black dotted line in Fig. 4(h) and confirms presence of invasive carcinoma with thickening of epithelium and vascularization and blood accumulation in the tumor. UBM cross sectional scan (Fig. 4(d)) shows tumor with relatively hyperechoic top and hypoechoic center. Regions of higher vascularization correlated to high signal intensity in PAI cross sectional scan (Fig. 4(e), arrows A and B).

3.4 Mucin light absorption effect on PAI and FLIm images

One of the animals from the precancer group presented a high accumulation of mucin in tissue around glandular structures confirmed in histology (Fig. 5(c)). Mucin membranes are naturally produced by epithelia to promote lubrication and cell signaling and act as a chemical barrier. Mucins are considered diagnostic markers of cancer and are often overexpressed in carcinomas [38] and have high absorption of 532 nm light [39]. As a result they may contribute to high PAI signal as seen in Fig. 5(d). Although the fluorescence intensity map (Fig. 5(a)) does not clearly provide information about the presence of mucin, CH1 lifetime map (Fig. 5(b)) shows a reduction in lifetime (black arrow).

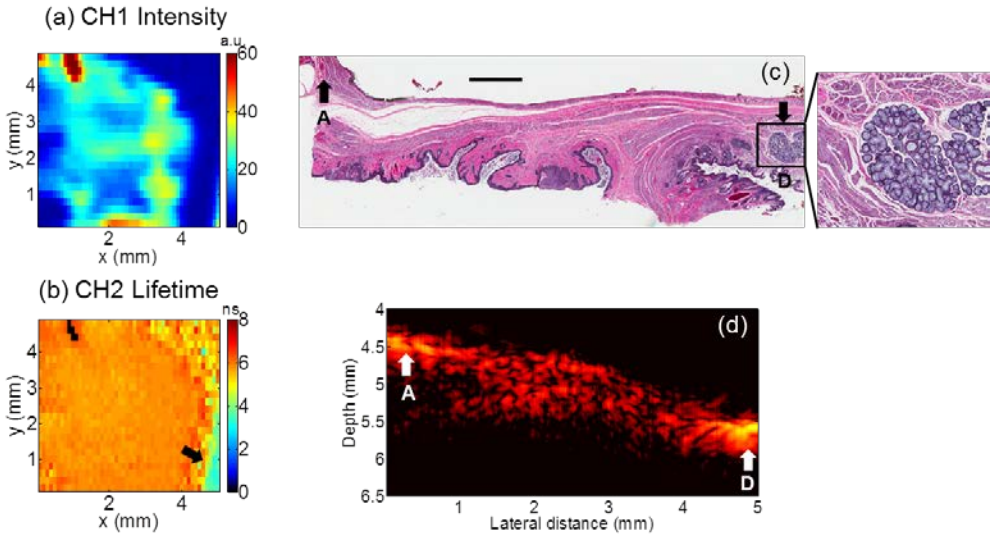

Fig. 5. FLIm, PAI and histology results from a precancer animal case showing mucin accumulation around glands in tissue. 2-D maps of fluorescence (a) intensity and (b) lifetime from CH1 (390/40 nm) showing lowering of lifetime in the region (black arrow) where mucin accumulation is seen in (c) H&E histology section (magnified region shown on right). (d) PAI cross sectional image showing high signal intensity (white arrows, A and D) corresponding to region with vascularization and mucin accumulation as seen in (c) (black arrows).

3.5 UBM for visualization of organized structure versus disruption of tissue architecture

Development and progression of tumor is often marked with disruption of tissue architecture including the epithelium, basement membrane, muscularis and adventitial connective tissue. Figure 6 shows UBM and histology results from normal and carcinoma hamster cheek tissue. The histology results show presence of intact tissue layers in normal case (Fig. 6(b)) and the same is observed in UBM cross sectional scan (Fig. 6(a)). The tumor case shows loss of distinct tissue layers with epithelial thickening (Fig. 6(d)) and disruption in tissue architecture is also seen in UBM with hypoechoic regions (Fig. 6(c)).

#193145 - $15.00 USD Received 1 Jul 2013; revised 9 Aug 2013; accepted 9 Aug 2013; published 26 Aug 2013

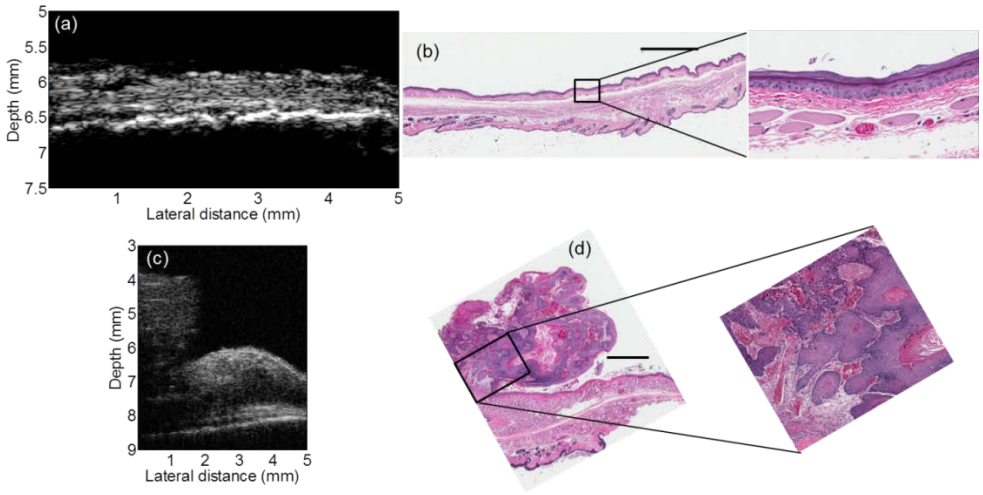

Fig. 6. UBM cross sectional images from (a) normal and (b) carcinoma case with corresponding co-registered H&E histology sections shown in (b) and (d) respectively. Tissue structural layers as seen in histology for normal case can also be seen in the UBM image. Similarly, loss of structural arrangement in tumor case is also observed in UBM image (c) which is confirmed in histology (d).

3.6 FLIm and UBM parameter distribution across distinct tissue groups

Figure 7 summarizes FLIm parameters (lifetime and LC-1) across all normal, precancer and carcinoma cases. The mean average lifetime values from all 5 normal tissue cases were 5.4 ± 0.6 ns and 4.6 ± 0.6 ns from CH1 and CH2 respectively, indicating small cross-sample variability. The precancer cases presented a slight increase in average lifetime values in both CH1 and CH2 (5.7 ± 0.6 ns and 5.4 ± 0.9 ns respectively) when compared with normal cases. However, the pixels associated with lesions visually observed at the tissue surface (Fig. 3(h)) presented a shorter lifetime values as well as a broader distribution of the LC-1 values in both emission channels. The average lifetime in CH2 corresponding to NADH emission provides the best discrimination between normal and precancerous tissue. The carcinoma case presented a broad distribution for time-decay values with two distinct regions. The pixels from the tumor region had a lower mean average lifetime for CH1 (3.4 ± 1.4 ns) and CH2 (3.3 ± 1.2 ns) when compared to the surrounding area (~5.7 ns). The fluorescence decay characteristics of the surrounding areas were comparable with those obtained from precancer tissue. Note that the LC-1 values are entirely negative for normal case while the distribution extends towards positive values for precancer and tumor cases.

Figure 8 summarizes the UBM RF data derived parameters (IB and E) across normal, precancer and invasive carcinoma cases. These parameters also show distributions that are markedly different across different tissue conditions. The integrated backscatter values from normal, precancer and tumor cases were –20.1 ± 6.6 dB, –31.0 ± 5.0 dB and –38.0 ± 5.0 dB respectively while the energy norm values were 0.054 ± 0.04, 0.014 ± 0.009 and 0.007 ± 0.004 respectively. IB values are observed to decrease in advanced lesions. Similarly, a decrease in E values is also observed along with narrowing of the overall distribution in precancer and carcinoma tissue when compared to normal tissue.

#193145 - $15.00 USD Received 1 Jul 2013; revised 9 Aug 2013; accepted 9 Aug 2013; published 26 Aug 2013

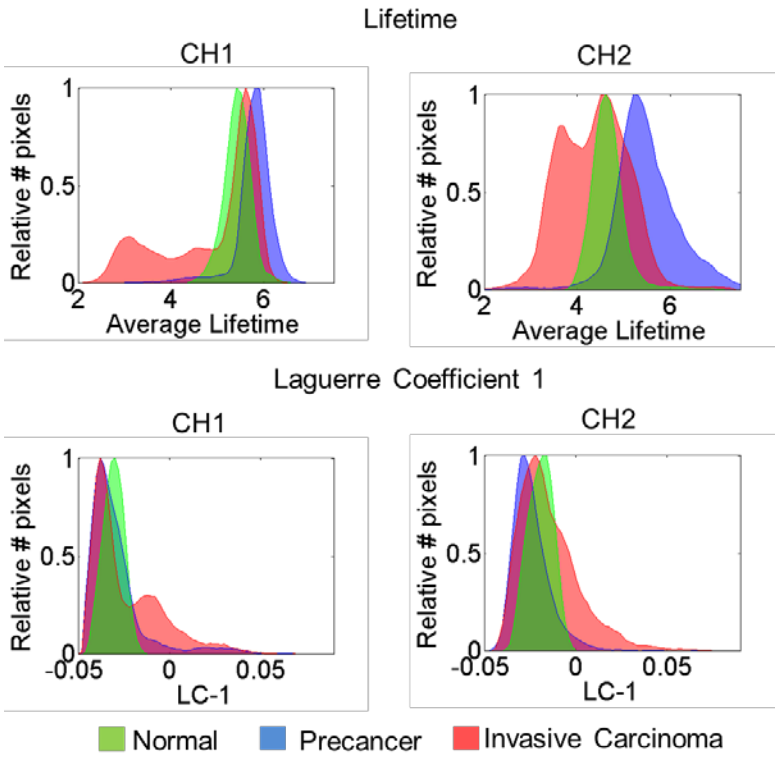

Fig. 7. Average lifetime values and LC-1 histogram distribution for all normal (5), precancer (3) and invasive carcinoma (4) cases from CH1 (390/40 nm) and CH2 (450/45 nm) fluorescence emission. Data shown is from the entire imaged region.

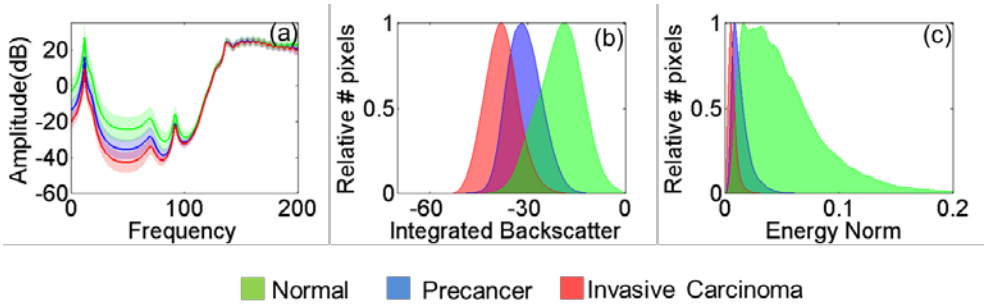

Fig. 8. UBM parameters computed from raw RF signals extracted from randomly selected regions of interest in UBM images representing normal, precancer and carcinoma treatments. (a) Backscatter coefficient function with standard deviation; histogram distribution of (b) Integrated backscatter (IB) computed from (a), and (c) Energy norm (E).

4. Discussion

This work reports the first application of a multimodal imaging technique combining FLIm, UBM and PAI for non-invasive detection of oral carcinoma *in vivo*. The imaging system has the capability of providing co-registered data from each of the three imaging modalities and hence allows for correlating molecular changes at the tissue surface with structural and functional changes in tissue depth. While each of the three modalities has distinct spatial resolution and depth of penetration, they can provide complementary diagnostic information

#193145 - $15.00 USD Received 1 Jul 2013; revised 9 Aug 2013; accepted 9 Aug 2013; published 26 Aug 2013

from tissue and enable cross-validation of results. A summary of the features provided by each modality as well as their synergistic potential is discussed below.

4.1 FLIm comparative analysis

FLIm measurements have shown that the three different tissue conditions (normal, precancer and invasive carcinoma) can be distinguished based on their average lifetime and LC-1 values. The lifetime values from all normal tissue cases were found to be longer in CH1 (5.4 ± 0.6 ns) relative to CH2 (4.6 ± 0.6 ns). This is indicative of normal tissue where the lifetime in CH2 is lower owing to fluorescence contribution from NADH with a lifetime of 0.5 ns in free-state and 2-3 ns in bound state [36] which affects the emission of collagen (5-6 ns). LC-1 values describe the slow decay component of the measured fluorescence signal. For all precancer cases, the lifetime values were higher than the lifetime values seen in the normal case. This increase in lifetime is in agreement with previous reports [40] that demonstrated collagen synthesis and cross-link formation in the tissue that is distantly or mildly affected by DMBA treatment used to induce breast tumors in rat. Increase in collagen cross-links has been associated with increase fluorescence lifetime [41]. Note that for the case shown in Fig. 3, lower lifetime values (~1-3.5 ns) were observed in both channels (CH1 and CH2) for precancer regions and may be because the region is closer to tumor tissue in biochemistry but is classified as precancer by the pathologist. The lower lifetime values are likely due to increased fluorescence from bound NADH due to higher metabolism in tumor/hyperplastic tissue as result of epithelial thickening. Bound NADH has a lower lifetime (~2.0 ns) than collagen (5-6 ns) [36]. This trend was recapitulated for tumor tissue which has lower collagen content as verified from histology and UBM results (Fig. 4) there by reducing the autofluorescence signal from collagen and hence lowering the overall lifetime value. For all cases with carcinoma, the tumor region had a lower lifetime of 3.4 ± 1.4 ns and 3.3 ± 1.2 ns from CH1 and CH2 respectively. An interesting observation was that LC-1 values can also delineate the tumor tissue regions where these values tend to be relatively higher (more positive) compared to normal tissue (Fig. 7). Results from the three different tissue cases suggest that LC-1 values become positive as to tumor development progresses. Overall, fluorescence lifetime and decay dynamics (LC-1) allow differentiating between normal, precancerous and carcinoma tissue where changes seen in these parameters can be attributed primarily to changes in collagen and NADH biochemistry upon 337 nm light excitation. However, these parameters are confined to the tissue surface (~250 μm depth) due to limited penetration of UV light in tissue. No information on tissue changes beneath the surface is available.

4.2 UBM comparative analysis

UBM was shown to complement the FLIm results as cross sectional images allows for the visualization of tissue structure and arrangement. Varying echogenicities in the UBM image allow identification of structural changes in tissue at distinct stages. For example, the organized microstructure of normal hamster cheek tissue including the epithelium and sub-epithelium connective tissue, muscle fiber mucosa, and adventitial connective tissue were clearly resolved. The UBM image of tissue with precancerous lesion (Fig. 3(d)) shows hyperechoic regions with epithelial thickening and collagen while pulsatile diverticulum appears as hypoechoic regions on the image. Moreover, carcinoma areas show hypoechoic regions due to collagen degradation as seen in Fig. 4(d). UBM images also provide information about overall changes in tissue architecture pertaining to disruption of tissue layers and tumor invasion (Fig. 6(d)). For example, disruption of tissue structure can be seen in the corresponding UBM image where loss of collagen and structure is seen as hypoechoic regions in the image. This feature is important for potential future clinical applications as disruption of basement membrane is associated with tumor invasion and metastasis.

#193145 - $15.00 USD Received 1 Jul 2013; revised 9 Aug 2013; accepted 9 Aug 2013; published 26 Aug 2013

This study also reports quantitative RF analysis of UBM data (Fig. 8) which show marked differences between different tissue types. Integrated backscatter (IB) values computed from the backscatter coefficient function in addition to the energy norm from randomly selected regions of interest in UBM images allowed for discrimination between normal, precancer and carcinoma tissue. The backscatter of ultrasound energy from a surface is dependent on the acoustic impedance mismatch between two media. Since the acoustic impedance is dependent on the density of the medium, it can be inferred that changes in tissue properties due to degradation of sample and/or changes in packing and arrangement of its constituent elements will be seen as variations in the amount of reflected/backscattered ultrasound energy. The IB values tend to decrease (more negative) as tumor progresses (Fig. 8(b)) as less ultrasound energy is backscattered from disrupted tissue. The energy norm quantifies the amount of absolute energy contained in a given region of interest in the UBM image. Energy norm values from normal tissue show a large distribution (Fig. 8(c)) due to signal arising from different intact layers in tissue while the distribution rapidly narrows as tissue structure is disrupted due to cancer development. Our results demonstrate that qualitative UBM images and quantitative RF analysis can provide insight in to tissue topology, structure and thickness that can help in understanding tissue pathology when coupled with other imaging modalities such as FLIm.

4.3 PAI comparative analysis

PAI imaging results from various cases showed that tissue areas with high density of small blood vessels (capillaries) are correlated to high PAI signal intensity. This can be seen in PAI images from all tissue types and are correlated with histological data. As a result, PAI data can provide information about angiogenesis and may help not only in identifying tumors areas which are often more vascularized than normal tissue but also regions of high metabolic activity that can be cross-correlated with FLIm results. Additionally, PAI coupled with FLIm measurements may also help detect the presence of mucin in tissue that is often overexpressed in carcinoma. Results from a precancer animal case with mucin expression shows that mucin leads to generation of high PAI signal intensity. Also, the presence of mucin was observed to change the overall fluorescence lifetime of tissue. Fluorescence lifetime and photoacoustic properties of mucin in relation to imaging of cancer have not been previously reported and may help in improving diagnostic potential of cancer imaging. The current study however, only reports a single case with mucin expression and a larger data set would be needed to evaluate the predictive value of PAI in imaging mucin for cancer diagnosis.

4.4 Challenges with current multimodal imaging system

Current results demonstrate the diagnostic and synergistic value of each of the three modalities integrated in to one system using a combined imaging probe device. However, the present implementation of the system limits the speed of acquisition due to the low repetition rate of the Nd:YAG laser used in PAI system (20 Hz) as well as that of the nitrogen laser used for fluorescence excitation (30 Hz). An upgrade of these laser systems is envisioned to not only reduce the duration of imaging but also enable simultaneous recording of imaging data from at least two imaging modalities. For example, FLIm and UBM data can be acquired concomitantly by replacing the current nitrogen laser with a solid state pulsed laser (such as Fianium UVP355, variable repetition rate, 355 nm) operating at a frequency comparable with UBM (500 Hz). PAI imaging results were able to detect regions of high vascularization and mucin accumulation on account of high intensity signal but with sub-optimal resolution of the tissue volume. The PAI illumination may need to be further optimized to improve imaging results. Additionally, a higher repetition rate laser (> 500 Hz) such as Nd:YLF pump laser may be employed to reduce imaging time while compromising on imaging depth. Although this work only presents qualitative results from PAI, it must be emphasized that clinical decisions are not based purely on quantitative evaluation of certain parameters, but also via

#193145 - $15.00 USD Received 1 Jul 2013; revised 9 Aug 2013; accepted 9 Aug 2013; published 26 Aug 2013

visualization of features (e.g. disruption of tissue structure as seen in UBM, or presence/absence of mucin and high vascularization as seen in PAI). Nonetheless, a more in depth analysis of PAI results from a larger set of animals is needed to explore its potential in understanding the functional properties of tissue and accumulation of mucin with respect to cancer development.

A multimodal diagnostic system such as the one reported here can generate a large number of diagnostic parameters/variables (e.g. fluorescence decay parameters at multiple wavelengths, UBM images and RF derived parameters). In order to reliably determine a small and robust subset of parameters that can complement each other for tissue discrimination, a more comprehensive study involving a larger set of animals is required. Current work presents representative results from different tissue cases and cannot assess the robustness of the system in classifying tissue types. A larger study will allow development of classification algorithms that use a combined set of fluorescence decay parameters (lifetimes and Laguerre coefficients) and parameters derived from a quantitative analysis of UBM-RF data (e.g. integrated backscatter coefficients and energy norm) for simultaneous assessment of tissue biochemical and morphologic features. The study, nonetheless, provides novel co-registered imaging results from FLIm, UBM and PAI for oral cancer diagnosis *in vivo*.

5. Conclusions

This study reports a multimodal system combining FLIm, UBM and PAI techniques using a unique scanning probe device to integrate the optical and ultrasonic energy delivery-collection pathways. The system was employed to image and evaluate oral carcinoma *in vivo* in a hamster model. Present findings demonstrate that biochemical, structural and functional properties of tissue can be evaluated synchronously using the presented system. FLIm results reported here were found in agreement with earlier studies [22–26] and show the ability of fluorescence decay parameters to resolve molecular changes at the tissue surface. Overall, tumor progression appears to be associated with decrease in fluorescence lifetime when compared with surrounding areas. It was also noted that the tissue surrounding the tumor or distantly exposed to carcinogen presented longer lifetime values than normal control tissues which can be attributed to increased collagen crosslinking. UBM provided complementary information on the tissue morphology and microstructure associated with such molecular changes. UBM gray-scale images showed hypoechoic collagen deprived regions in tumor and allowed for qualitative detection of basement membrane disruption. Moreover, this study also demonstrated analysis of UBM radio-frequency data as an additional quantitative means of differentiating between different tissue types. PAI was able to detect areas with high vascularization within the tissue and tumor volume. An important observation is the ability of PAI to detect mucin accumulation in precancerous tissue which was complemented by observing a reduction in the fluorescence lifetime. In summary, the case studies show the potential of combined FLIm, UBM and PAI for providing synergistic data for enhanced cancer detection. Future work will focus on acquiring data from a larger set of animals to explore the capability of this multimodal technique to identify, delineate and classify different cancer related pathologies.

Acknowledgments

This work was supported by NIH grants R21-RR025818 and R01-HL67377 and the training program in molecular imaging grant 5T32EB003827. The authors acknowledge K. Kirk Shung, Jonathan Cannata, and Hao-Chung Yang for providing the ultrasound transducer used in this study.

#193145 - $15.00 USD Received 1 Jul 2013; revised 9 Aug 2013; accepted 9 Aug 2013; published 26 Aug 2013